Understanding And Modeling CMAS And Thermal Barrier Coating Interaction Under Thermal Gradients

Thomas Brunet, Thibaut Archer, Alice Dolmaire, Michel Vilasi

HTCPM 2024
June 9-14 2024 in Les Embiez Island (France)

Publication in the proceedings of the conference (no review)

Understanding And Modeling CMAS And Thermal Barrier Coating Interaction Under Thermal Gradients

T. Brunet [a], T. Archer [a], A. Dolmaire[b], M. Vilasi[c]

[a] DMAS, ONERA, Université Paris-Saclay, F92322 Châtillon, France
[b] DMAS, ONERA, Université Paris-Saclay, F91123 Palaiseau, France
[c] Institut Jean Lamour, Université de Lorraine, Campus Artem, 2 allée André Guinier - BP 50840, 54011 NANCY Cedex
thomas.brunet@onera.fr, thibaut.archer@onera.fr, alice.dolmaire@onera.fr, michel.vilasi@univ-lorraine.fr

Abstract. When operating at very high temperatures (starting from 1200°C), thermal barrier coatings (TBCs) start interacting with oxide particles such as CMAS, found in sand or volcanic ashes. Namely, CMAS can infiltrate the TBC and tamper the thermal and mechanical properties of said TBC, leading to its deterioration. This study aimed to understand the interaction between yttria partially stabilized zirconia (YSZ) TBCs and CMAS particles under a thermal gradient. The TBC was made through an EB-PVD process. The experimental study was conducted with a laser rig. TBC samples were heated up to 1200°C and exposed to a cylinder-shaped CAS deposit for different durations. It was observed that the infiltration is a rather quick phenomenon, while the dissolution of the TBC and the precipitation of the crystalline phases worked on a longer timeline. Both phenomena can then be considered uncoupled under these test conditions and modeled as such. A heat transfer model was implemented as to better understand the different phenomena happening. The model was fitted to experimental data through a test-calculation dialogue.

Keywords Thermal Barrier Coating, CMAS, Yttria-stabilized Zirconia, Test-calculation dialogue

Introduction

As engine manufacturers aim to increase operating temperatures, there is a growing need for ways to protect metallic components within the engine. This is especially the case for high-pressure turbine components. One way to address this issue is to add a ceramic layer on top of the metal substrate, which acts as an insulator, called a thermal barrier coating (TBC). The most widespread technology is the yttria partially stabilized zirconia (YSZ) with 8 wt.% yttria deposited through an electron-beam phase vapor deposition (EB-PVD) process, as it benefits from a good strain tolerance and a relatively low thermal conductivity (~ 2 W/ (m.K)) [1].

However, previous studies show that upon reaching certain temperatures, TBCs start interacting with oxides particles named CMAS (for Calcia Magnesia Alumino-Silicates), quickly leading to their deterioration [1, 2]. Those oxide particles can be encountered either when flying over a desertic or volcanic region. Two types of CMAS-induced deterioration can be highlighted. The first one is of thermo-mechanical nature: upon melting, CMAS particles form a viscous glass-melt which can then infiltrate the TBC, especially when dealing with EB-PVD TBC which are prone to infiltration due to their porous microstructure. The infiltrated TBC has a diminished compliance to stress and usually ends up cracking upon cooling [3 - 6]. The second one is of thermo-chemical nature: a chemical interaction takes place between the TBC and the melt, leading to a precipitation of certain crystalline phases [3, 7]. The microstructure of the TBC changes and so do a number of its mechanical and thermal properties.

As highlighted by different authors in the literature [1, 8], CMAS composition heavily depends on the geographical position and can be more complex than the usual ternary CaO-MgO-Al_2O_3-SiO_2 (e.g. there can be traces of iron or sodium oxides). In an attempt to simplify the physico-chemical study of the CMAS/TBC interactions, that is to say in the hope of obtaining reaction products with a simple microstructure, easy to interpret, a synthetic yet simplified CAS of composition 61.5SiO_2-15Al_2O_3-23.5CaO wt.% was chosen. It also melts at quite a low temperature (~1200°C) [9] making it possible to conduct the experiments on the laser rig while avoiding the deterioration of the TBC solely from the heat treatment.

As of today, numerous studies have been conducted in an isothermal configuration, using a furnace [3, 7, 10]. A few studies however have started to highlight the importance of thermal gradients [4, 5, 11, 12], using either laser or burner rigs. According to these studies, thermal gradients will affect multiple aspects of the study. For example, a smaller depth of infiltration, a shorter lifespan of the component during thermal cycling or a greater driving force for delamination can be observed. These studies were sometimes coupled with thermo-mechanical models, in which the heat transfer issue is not addressed: a simple 1D thermal gradient is usually imposed as an input of the model [11].

The present study aims to better understand the interaction between CMAS and TBCs under a thermal gradient through the implementation of a test-validated model. To this end, a laser device developed at ONERA is used and a heat transfer model is being developed. To date, the first results related to this modeling work concern the study of LASER/material interactions without CMAS deposition. The next modeling step will consider the interactions resulting from the presence of a CMAS deposit and will be progressively implemented. To this end, experiments including CMAS will first be conducted without a thermal gradient and the studied configurations will gradually become more complex.

Experimental methodology

a) Laser rig facility

The samples were tested in a laser rig facility, shown in Fig. 1, designed to impose certain thermal gradients through the TBC thickness. It consists in a 1kW CO_2 laser and an air stream. The laser is used to heat up the upper surface of the sample while the air stream cools down the bottom surface. Both the power amplitude of the laser and the air flow can be modulated, thus ensuring different experimental conditions can be obtained (namely different temperatures on the TBC surface and different value of thermal gradient through the TBC's thickness). A top-hat optics is used to homogenize the gaussian laser flux incident on the surface of the sample. The resulting flux field in Fig. 2 is obtained thanks to a flux analyzer.

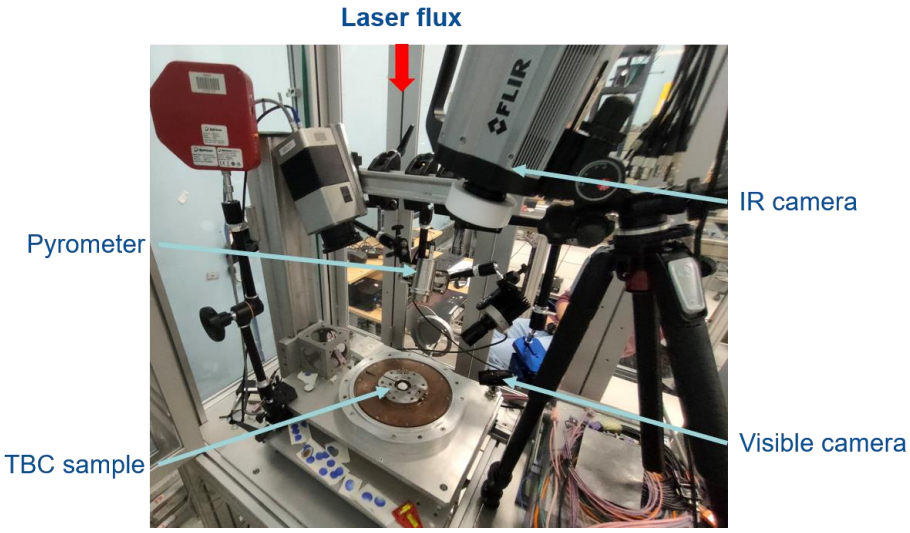

Fig. 1 Laser rig facility present at ONERA

Multiple instruments permitted a comprehensive monitoring of the temperature through the sample. For the upper face, both an 8 µm pyrometer and a LWIR camera equipped with a 9 µm pass-band filter were used. The pyrometer focused on the center of sample surface while the camera was used to map a thermal field. A type K thermocouple was inserted inside a drilling in the middle of the metal substrate. A bicolor pyrometer was used to monitor the temperature in the center of the bottom surface, said surface being coated with an AREMCO 840MX high-emissivity coating. This coating ensured a greater emissivity, thus providing greater confidence in the data obtained with this pyrometer.

Finally, in the cases for which CMAS were added, a blue LED lighting and a visible camera were used to follow the shape of the CMAS deposit on top of the sample. A MWIR camera was also added to monitor possible thermal gradients through the CMAS deposit. Both theses cameras were set up as to provide a transverse view of the surface.

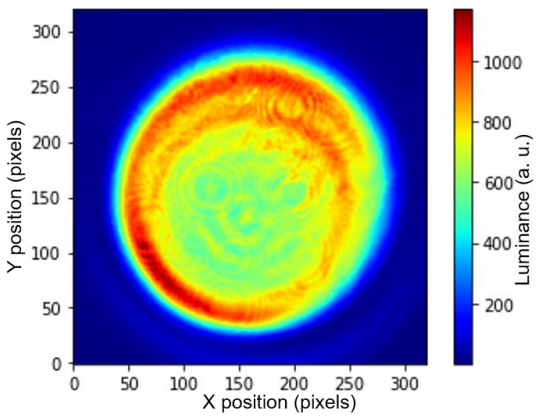

Fig. 2 Average laser heat-flux field (in DL) over 30 seconds at 375W

b) Samples description

The samples consist in a 7YSZ deposited TBC on a NiPtAl bond coat linked to a metallic superalloy substrate AM1 [2]. The TBC is deposited through an EB-PVD process and is around 150 µm thick. The superalloy is a few millimeters thick. The zirconia is mostly tetragonal, however, because of a heat treatment, part of it reprecipitated in a monoclinic phase. Samples used were thermally cycled a hundred times (each cycle lasting an hour) at 1150°C prior to the experiments with a CAS deposit.

c) CAS elaboration

The synthetic CAS was obtained according to the protocol described by F. Perrudin in his thesis [13]. It was crushed in a fine powder and sieved with a 60 µm sieve. The powder was then pressed in a cylindrical matrix at around 50MPa for about a minute. A mass of 200 mg of CAS is used for each cylinder. This mass ensures that there is enough CAS to fully infiltrate the whole TBC according to various papers in the literature [10, 11]. The cylinders measured around 8mm in diameter and were about 2 mm thick. They then underwent a heat treatment of 720°C for 8h in a furnace to make them less brittle. The cylinders had a density of 2.61 g/cm^3 (helium pycnometry analysis), that value was not affected by the heat treatment. This made it possible to transport the cylinders to the laser test rig without them falling apart.

d) Design of experiment

a. Design without CAS

A few first experiments were conducted without CAS deposits to ensure adequate laser settings. For those experiments, an air flow of around 200 L/min was used to cool down the bottom surface of the samples. A TBC sample was exposed to different combination of laser power amplitude and air-cooling configurations for a few minutes each time (for each configuration, at least 5 min of data were recorded once the temperature was stable enough and reached its final value). The different combinations are summarized in Table 1. Data extracted from those experiments were then used to fit a first simplified model, without CAS. A 3D heat transfer finite element model representing a 120° angle cut of the sample was created in Abaqus finite element software. A few hypotheses were considered: conductivities are considered isotropic and homogeneous, they only vary based on temperature. Same goes for the different emissivity parameters. The laser power amplitude is considered homogeneous on the surface of the sample. The identification of

the parameters of the problem were made in steady-state configurations. Transient analyses were then performed to validate the identified model.

Table 1.
Different configurations studied for the cases without CAS deposit

Configuration n°	1	2	3	4	5	6	7	8	9
Laser amplitude (W)	100	100	100	200	200	200	300	300	375
Air flow (L/min)	200	100	0	0	100	200	200	100	200

b. Design with CAS

Two samples were studied in fairly identical configurations: a CAS cylinder was mounted on the center of both samples. Two different treatments were then studied.
For the first sample, a heating phase during which the laser power went from 0 to 300W in around 15 min, after which an infiltration phase started. It consisted in holding the power at 300W for another 30 minutes. After this hold, the laser was shut down.
For the second sample, the laser power was instantly set to 300W and that amplitude was held for 30 minutes after which the laser was shut down.
In both cases, no air flow was added to cool down the bottom surface.

e) Microstructural characterization

Infiltrated samples were examined with X-Ray Diffraction (PANalytical - Empyrean diffractometer, Cu-Kα radiation) to determine which crystalline phases had been formed.

They were then embedded in epoxy. Polished cross-sections were provided and covered with a very thin layer of graphite in order to be studied with a scanning electron microscope (SEM/BSE). EDS analyses were also performed as to follow the distribution of elemental compositions throughout the infiltrated TBC thickness.

Results

a) General observations made in absence of CAS deposit

The first observation that was made, prior to the addition of CAS deposit, was about the shape of the thermal field on the TBC surface. Both spatial and temporal standard deviation in terms of temperature were within a 20°C range which is acceptable. Having a homogeneous thermal field is indeed proof that the top-hat is well set and that the sample is correctly placed. It also provides data that is easier to interpret and that can be reproduced more easily.

b) Qualitative observations with a CAS deposit

As explained earlier, a cylindrical CAS deposit was added on the surface of the sample. This deposit measured 8 mm in diameter and was 2 mm thick. Upon heating with a laser, the deposit quickly melted and formed a sphere which had a small contact surface with the TBC below it. The sphere then slowly spread out, infiltrating the TBC as it spread. It went from a sphere to a hemisphere - within 7 minutes for the second sample - and ended up looking like a flattened bell curve. Some of the centermost part of this so-called CAS bell curve broke during cooldown.
Transitions between the different shapes described previously can be associated with certain events that were obtained on the thermograms, such as the deposit temperature going from 1550°C up to 1700°C between the sphere formation and its following spreading on the TBC.
Thanks to the LWIR camera filming from above and the visible camera filming from the side, it was possible to follow the size of the infiltrated zone throughout time. This can help study the kinetics of the chemical reaction later on as it gives a better measure of how long a certain part of the TBC was infiltrated by the CAS deposit.

c) CAS infiltration

BSE analysis in the center region of the sample shows a fully infiltrated TBC. In fact, the TBC is fully infiltrated on a large portion of the infiltration zone. On the extremities of the infiltration zone however, the TBC is only partially infiltrated. The infiltration front has an elliptical shape, as can be seen in Fig 3, indicating that multiple intercolumn gaps are filled at the same time (it is not necessary for the previous gap to be filled before starting to fill other ones). By linking the observations from the previous paragraphs with the BSE analysis, it can be concluded that in the studied configuration, it takes around 10 minutes at 1200°C for the CAS to fully infiltrate the 150 µm-thick TBC. This is consistent with the observations from [10]. Further EDS analysis were performed on the infiltration front in order to check whether any elements from the CAS deposits were able to infiltrate the TBC further than what could be seen on the BSE observations. No elements (Ca, Al or Si) could be observed further than the limit determined through BSE analysis, thus confirming this infiltration front. It was especially important to verify this was true for the calcium, as it contributes to increase the fluidity of the glass network and in consequence, its capability to infiltrate the TBC [1]. Finally, in the fully infiltrated zones, it can be observed that the TBC is no longer adherent to the bond coat, really long delaminations can be seen which are not present in the sane regions.

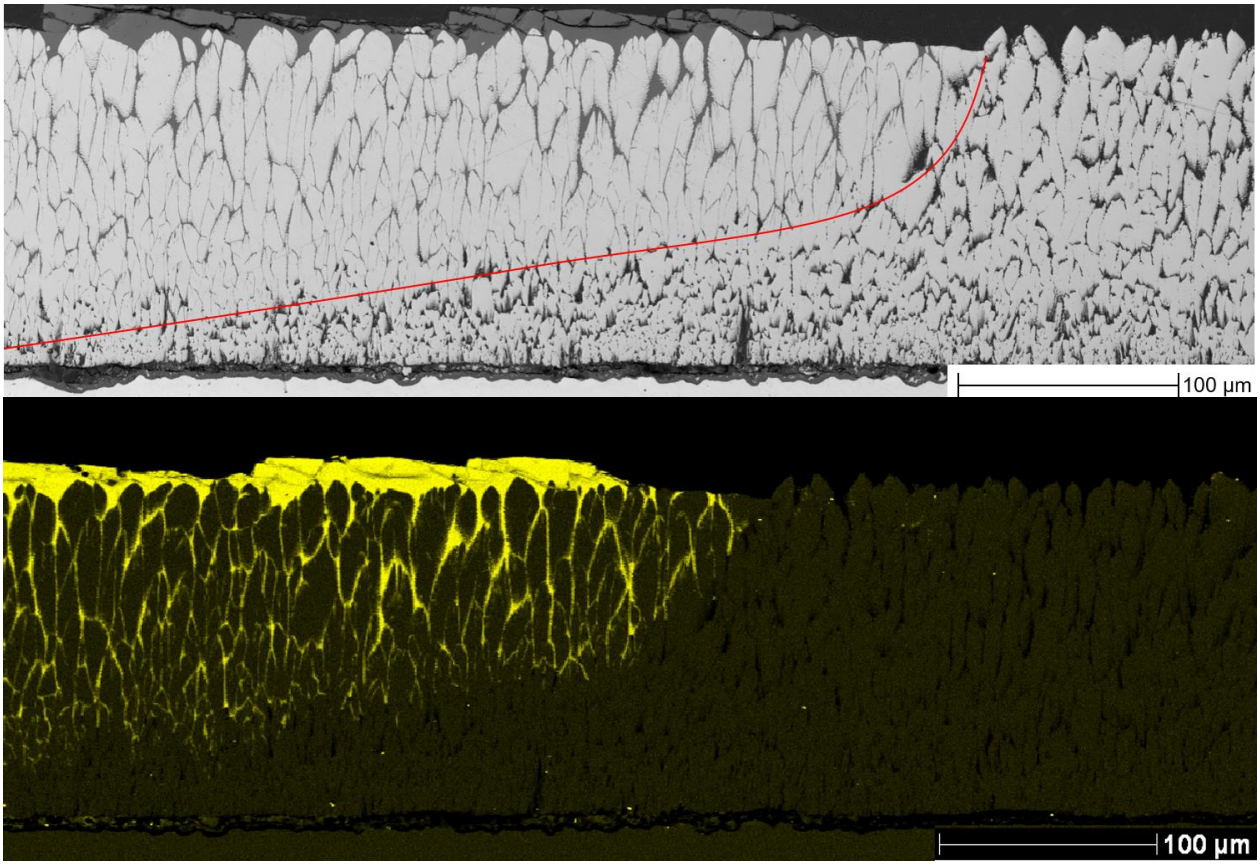

Fig. 3 (Upper) BSE image of the frontier (added in red) between the infiltrated (right side) and the sane region (left side) of the TBC (Lower) EDS elemental cartography of calcium for the corresponding region

d) Interaction between CAS and TBC

XRD analysis only showed presence of both tetragonal and monoclinic zirconia., hinting at the fact that no CAS had formed crystalline phases during the experiments. This hypothesis was nuanced with SEM/BSE imaging which showed mostly two contrasts: a white phase corresponding to the TBC and a dark gray phase corresponding to amorphous CAS. However, the presence of two more phases could be noted, though in small and located amounts, near a few column tops. EDS semi-quantitative analysis, shown in Fig. 4, highlighted the elemental variations of those phases and gave some insight concerning the composition: the first one, of clearer contrast and enriched in zirconia proves the TBC started to dissolve. A second darker phase is enriched mostly in aluminum and can appear as far as 100 µm from

the TBC. This seems to be equivalent to what Vidal-Setif et al. observed in [10], in which case the clearer phase corresponds to the monoclinic $Ca_2Zr(Y)Si_4O_{12}$ while the darker phase is the anorthite $CaAl_2Si_2O_8$, which is identified thanks to its needle-like shape. It should be noted that these phases only appear in the center of the interaction zone, where CAS could infiltrate the TBC really early on during the experiment. This result confirms that the infiltration and chemical interaction between TBC and CMAS can be treated as two subsequent events. Furthermore, no diffusion of zirconium or yttrium through the glass region of the CAS was observed. Finally, a third phase can be observed. The elemental maps show that this third phase is enriched in calcium but seems aluminum depleted. This differs from previous observations in [10] which did not mention the formation of this phase. According to the phase diagram for the CAS ternary which can be seen in [7], this phase could consist of pseudowollastonite. Indeed, the initial composition corresponds to that of the eutectic system which leads during cooling to the precipitation of the following three phases: anorthite, pseudo wollastonite and tridymite.

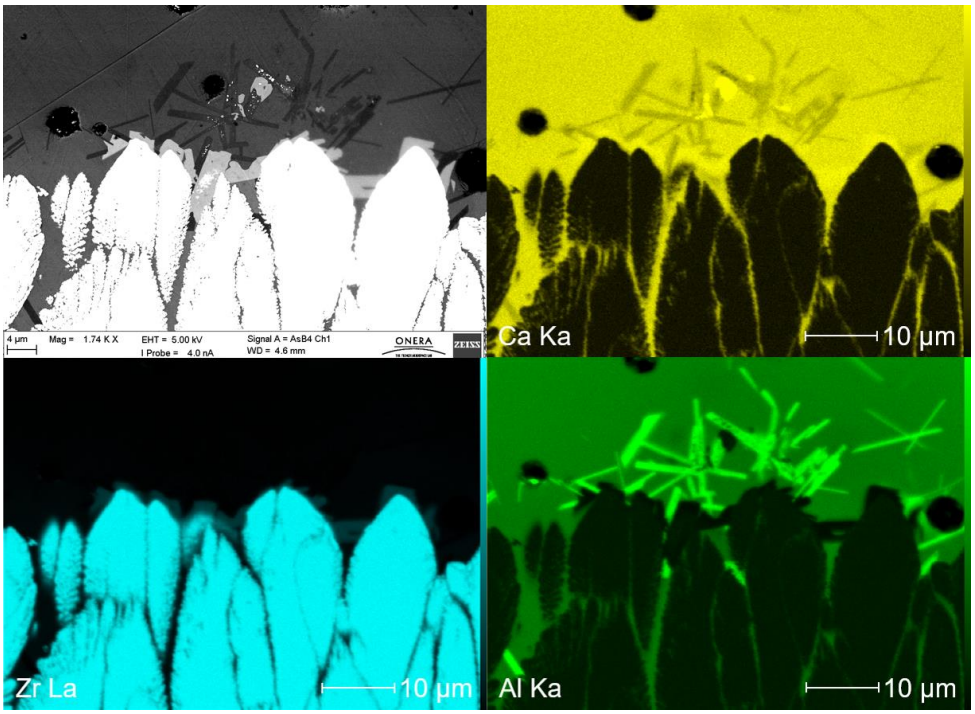

Fig. 4 SEM/BSE image and EDS elemental maps (Ca, Zr and Al) in the center region, near the top of the columns

Discussion

a) Modeling of the heat transfer problem and implementation of the test-computing dialogue

In order to better understand the interactions at stake, a heat transfer model of the problem has been implemented. Since both thermo-mechanical and chemical degradations are driven by the temperature changes, it is crucial to get a model as accurate as possible. It was first decided to create a model in absence of CAS/CMAS and to then increase the complexity gradually.

Upon completion of the model (described in the previous paragraphs), a numerical sensitivity analysis was conducted in order to determine, for each parameter in the model, whether they could be identified through a test-calculation dialogue or not, using experimental data gathered from configuration 1 to 9 described previously. In the end, six parameters were studied: surface laser power amplitude, air flow, emissivity of both TBC and coating used for the bottom face and thermal conductivity for the metallic substrate and the ceramic TBC. The experimental data obtained with the backside pyrometer and the LWIR camera on the front side were used.

The test-calculation dialogue was implemented using both the Abaqus model and a Python script. The goal of the dialogue was to minimize a certain cost function, defined in Eq. 1, assessing the numerical distance between the computed results and the experimental data.

$$\begin{cases} \chi = \omega\chi_{TBC} + (1-\omega)\chi_{Pyrometer} \\ \chi^2_{TBC} = \dfrac{\sum_{i\in TBC}\left(T_{exp,i} - T_{comp,i}\right)^2}{N_{points}} \\ \chi^2_{Pyrometer} = \left(T_{Pyrometer,exp} - T_{Pyrometer,comp}\right)^2 \end{cases} \quad (1)$$

In the first equation of Eq. 1, ω corresponds to a weight and its value is thus comprised between 0 and 1. The algorithm ended up giving convincing results, as the average numerical temperature distance was less than 10°C, which is lower than the standard deviation of temperature that could be experimentally be observed when maintaining a 375W laser amplitude for 10 minutes. A residue field, shown in Fig. 5 was computed in order to see the error made for each point of the mesh. It can be observed on this field that the experimental results obtained for configuration 9 presented an inhomogeneity: the TBC was hotter on the y=0 axis than on the other side of this third of the sample.

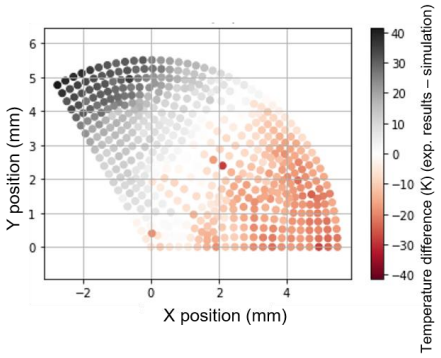

Fig. 5 Temperature residue: difference in temperature between the experimental and optimal calculated case – Configuration n°9 – Experimental results are projected on the computational mesh

It has also been made possible to find the optimal parameters with this method while including different configurations as inputs. In that case, the cost function becomes Eq. 2:

$$\psi = \sqrt{\sum_{i=1}^{N_{configuration}} \chi_i^2} \quad (2)$$

This last study allows for heightened confidence in the results obtained. It was for example used to assess the first three configurations together, better supporting the value obtained for the laser power amplitude, which has to be the same between those cases (100W).
The model was finally tested in a transient configuration and yielded results which were consistent with the experimental counterpart, thus validating the use of the proposed model.

b) CAS behavior

It is first observed that upon melting, the CAS cylinder forms a sphere before spreading out. It can be said that the deposit goes through a non-wetting stage, which was already observed by Yang et al. in [14], although their working conditions were slightly different, the temperature was set at only 1166°C and the CAS composition which was different. The expansion rate of the sphere seems to be slowing down over time, which would be consistent with the fact that the intercolumn gaps are being filled: as the melt expands, the number of intercolumn gaps being infiltrated increases, thus reducing the quantity of CAS available for expansion. It is also observed with the BSE analysis that it is not necessary to fully infiltrate gaps before continuing the expansion, as can be seen on Fig.3. However, all the gaps that are exposed long enough to the melt will end up fully infiltrated.

Conclusions

A preliminary study without CAS deposits was conducted as a less complex configuration. It was then modeled and experimentally validated. It involved multiple configurations with laser powers varying from 100 to 375W and an air-cooling flow from 0 to 200 L/min.

The infiltration process of synthetic CAS deposited on a 7YSZ (EB-PVD) TBC was then investigated using a laser rig facility. In absence of cooldown on the bottom face of the sample, the conditions were quite close to an isothermal testing. For all the tested configurations, the TBC was exposed to molten CAS for around 30 minutes. This ensured complete infiltration in the center of the samples. The deposit shape changed throughout the study: it went from a cylindrical compact deposit to a sphere of molten CAS prior to spreading on the surface.

SEM/BSE analysis were conducted in order to study the infiltration process of the CAS melt inside the TBC. An ellipse-shaped infiltration front was observed showing that multiple intercolumn gaps can be filled at the same time.

Chemical interactions between CAS and TBC were studied with DRX, BSE and EDS analysis. It showed the formation of three phases, two of which were accounted for in [10]: a monoclinic phase directly linked to the dissolution and reprecipitation of the TBC and an anorthite phase, consequence of the first phase formation. Those phases were present in such small quantities (only on a handful of columns) that they couldn't be detected through XRD.

Future work should include the study of CAS infiltration under thermal gradient as well the implementation of a new model taking CAS infiltration and chemical interaction with the TBC into account.

Acknowledgements

The authors would like to thank Dr Aurelien Joulia from Safran Tech for providing the samples, Nicolas Horezan and Quentin Barres for their expertise with SEM analysis as well as Maria Tsoutsouva for her help with XRD works. This work was supported by the French Innovation for Defense Agency (AID).

References

1. Gaudin, M. et al., Trends and Perspectives in Mitigating CMAS Infiltration in Thermal Barrier Coating. In: Pakseresht A, Amirtharaj Mosas KK, eds. *Ceramic Coatings for High-Temperature Environments*. Engineering Materials. Springer, Cham; 2024:37-85.
2. Vidal-Setif MH, et al., Calcium–magnesium–alumino-silicate (CMAS) degradation of EB-PVD thermal barrier coatings: Characterization of CMAS damage on ex-service high-pressure blade TBCs, *Surface and Coating Technology*. 2012;208:39-45.
3. Krämer S, et al., Thermochemical Interaction of Thermal Barrier Coatings with Molten CaO–MgO–Al2O3–SiO2 (CMAS) Deposits, *Journal of the American Society*. 2006;89:3167-3175.
4. Sundaram S, et al., The Influence of Transient Thermal Gradients and Substrate Constraint on Delamination of Thermal Barrier Coatings, *Journal of Applied Mechanics*. 2013;80:1-13.
5. Qian G, et al., Effects of thermal gradient and residual stresses on thermal barrier coating fracture, Mechanics of Materials. 1998;27:91-110.
6. Levi C, et al., Environmental degradation of thermal barrier coatings by molten deposits, *Materials Research Society*. 2012;37:932-941.
7. Poerschke D, et al., Equilibrium relationships between thermal barrier oxides and silicate melts, *Acta Materialia*. 2016;120:302-314.
8. Bansal NP, Choi SR, Properties of Desert Sand and CMAS Glass, *NASA Report*. TM 2014-218365
9. Levin, E.M., et al., *Phase Diagrams for Ceramists, Volume I*. Columbus, OH.: The American Ceramic Society; 1964.
10. Vidal-Setif MH, et al., Microstructural characterization of the interaction between 8YPSZ (EB-PVD) thermal barrier coatings and a synthetic CAS, *Surface and Coating Technology*. 2014;239:41-48.
11. Jackson RW, et al., Interaction of molten silicates with thermal barrier coatings under temperature gradients, *Acta Materialia*. 2015;89:396-407.
12. Drexler J, et al., Thermal-gradient testing of thermal barrier coatings under simultaneous attack by molten glassy deposits and its mitigation, *Surface and Coatings Technology*. 2010;204:2683-2688.
13. Perrudin F, Etude de la dissolution de diverses terres rares dans des liquides silicatés (CMAS) de composition variable – Contribution au développement des barrières thermiques en ZrO2-RE2O3 (RE = La-Lu), 2018.
14. Yang SJ, et al., Surface roughness affects metastable non-wetting behavior of silicate melts on thermal barrier coatings, *Rare Metals*. 2022;41:469-481.